R&D NOTE

Simulation of Liquid Water Breakthrough in a Nanotomography Reconstruction of a Carbon Paper Gas-Diffusion Layer

P. Rama
Intelligent Energy Ltd., Charnwood Building, Holywell Park, Ashby Road, Loughborough, Leicestershire LE11 3GR, U.K.

Y. Liu and R. Chen
Dept. of Aeronautical and Automotive Engineering, Loughborough University, Leicestershire LE11 3TU, U.K.

H. Ostadi and K. Jiang
Dept. of Mechanical Engineering, University of Birmingham, Birmingham B15 2TT, U.K

Y. Gao and X. X. Zhang
Dept. of Engineering, University of Liverpool, Liverpool L69 3GQ, U.K.

R. Fisher and M. Jeschke
Technical Fibre Products Ltd., Burneside Mills, Kendal LA9 6PZ, U.K.

DOI 10.1002/aic.12581
Published online March 31, 2011 in Wiley Online Library (wileyonlinelibrary.com).

Keywords: Polymer electrolyte fuel cell, gas-diffusion layer, porous flow simulation, lattice Boltzmann, X-ray nanotomography, microscopic flow, two-phase flow, pore-size distribution, liquid intrusion, hydrophobic, hydrophilic

Introduction

The gas-diffusion layer (GDL) of a polymer electrolyte fuel cell (PEFC) serves as an electron-conducting porous layer which simultaneously distributes reactant gases evenly to the adjacent catalyst layer (CL), and plays a crucial role in transporting excess liquid water from within the cell. Carbon paper is a common base material for the GDL which can be treated with a wet-proofing agent in order to render its internal porous structure partially hydrophobic and partially hydrophilic, thereby facilitating liquid-water transport. The GDL is a well-researched component of the PEFC from a macroscopic point of view, but one which due to the diminutive size of its porous features has been difficult to fully understand at a microscopic level through *in situ, ex situ* and computational techniques. What is of great interest for optimized fuel-cell performance, longevity and cost is the nature of the relationship between actual porous structure, hydrophobicity and liquid transport. The purpose of this feasibility study is to apply and report a numerical technique which newly combines a digitally reconstructed three-dimensional (3-D) model of the carbon paper GDL that is acquired directly through X-ray nanotomography with a 3-D two-phase lattice Boltzmann numerical model in order to simulate liquid-water transport into it.

To date a vast number of 1-D, 2-D and 3-D two-phase isothermal and nonisothermal numerical models of the PEFC based on the macrohomogeneous treatment of porous structures have been developed and applied in order to predict the general movement of liquid water and the distribution of reactant species within the cell.[1,2] These models satisfy the need to broadly understand the mechanisms that govern two-phase transport in the PEFC as a multilayer assembly, but cannot clarify how gases and liquids infiltrate through the actual structures of fuel-cell materials as manufactured by virtue of their macrohomogeneous treatment of structural properties. Indeed, they depend on semiempirical relationships such as that between capillary pressure and pore water

Correspondence concerning this article should be addressed to P. Rama at pratap.rama@intelligent-energy.com.

saturation in order to superficially predict the infiltration of liquid through the GDL.[3] To improve the understanding of the relationship between two-phase transport and actual geometric and surface features of porous fuel cell structures, an alternative approach to macrohomogeneous modeling has to be developed and applied which is based on capturing transport as a microscopic phenomenon at pore scale.

The lattice Boltzmann (LB) technique is one that has been increasingly exploited in recent years to simulate single-phase and two-phase transport in porous fuel-cell materials. Principally, the technique simulates fluid flow by tracking the movement of fictitious particles around a lattice using statistical arguments. A short review of recent studies is provided herewith.

Wang and coworkers simulated liquid-water distribution in a stochastically reconstructed 3-D microstructure of a carbon cloth GDL with randomly distributed mixed wettability (80 and 140°), and fully hydrophobic (140° contact angle) surface properties.[4,5] Their results illustrated qualitatively that the liquid-water distribution for a given level of saturation is strongly dependant upon wettability, which can change as GDLs are degraded during service life. Niu et al. conducted a similar study which examined the transients of the liquid-gas transport process through a stochastically reconstructed 3-D model of the GDL, analyzing the effect of pressure drop across the GDL and wall hydrophobicity.[6] Koido et al. applied the LB model with a microfocal X-ray CT image of carbon paper to simulate the relative permeability of the liquid and gas phases and compared the measured capillary pressure with calculated data for a pore water saturation of 0.1, with both sets of results exhibiting general agreement.[7] A similar study presented by Park and Li simulated orthogonal permeability and unsteady droplet movement through a 2-D image of a carbon paper GDL.[8] Hao and Cheng simulated the dynamic behavior of water droplet formation and removal in the gas channel of a PEFC.[9] Their study concluded that by increasing the gas-flow velocity in the channel and by increasing the hydrophobicity of the GDL, it may be possible for liquid droplets that emerge on the GDL surface to detach much sooner, thereby demonstrating the potential to delay flooding effects.

In the authors' previous work, a 3-D LB scheme was progressively developed and applied to examine gas transport through 3-D models of the fuel-cell GDL which are digitally reconstructed via X-ray nano- and microtomography. The authors successfully applied the technique to predict gas-phase permeability through uncompressed carbon paper,[10] uncompressed carbon cloth,[11] compressed carbon cloth,[12] and multicomponent single-phase transport through carbon paper.[13] The principal difference between these efforts in comparison to the contributions of other studies in the literature is that the author's previous work incorporated 3-D models that were generated directly from carbon-based GDLs as manufactured using X-ray tomography, as opposed to employing stochastically-reconstructed models.

In this research, a new two-phase 3-D LB model has been developed to simulate liquid infiltration in a digitally-reconstructed structural 3-D model of the GDL via X-ray nanotomography. To demonstrate the feasibility of the approach, the study here focuses on the initial breakthrough of liquid water fronts through a finite thickness of the GDL structure at two different levels of surface hydrophobicity represented by two different contact angles. In order to visualize the evolution of liquid intrusion as a 3-D phenomenon within the captured structure, a range of liquid intrusion pressures are examined, while the results of volumetric intrusion are also discussed.

Model Description

The specific objectives of the current feasibility study are:

1. To develop a 3-D two-phase lattice Boltzmann (LB) numerical model;
2. to create a direct digital model of the carbon paper GDL through X-ray nanotomography, and;
3. to numerically simulate and visualize the initial breakthrough of liquid water in the GDL using the newly-developed two-phase LB model.

A single region of interest from the reconstructed GDL sample is taken after the X-ray imaging process and then used repeatedly with the LB model for the numerical study.

This section provides a description of both the X-ray nanotomography image generation and digital reconstruction process, and a numerical explanation of the new two-phase LB model. It is noteworthy that for this work the gas phase is assumed to be air and treated as a mixture.

X-ray Nanotomography

The nanotomography process involves three principle steps; image acquisition, image processing and digital reconstruction. The technique applied is fundamentally the same as that applied in the previous work, with the notable exception that different equipment is used here in order to capture the nanoscale porous features as opposed to microscale features.[10–13]

A 3-D digital model of the true heterogeneous porous structure of an actual GDL sample is initially generated using 200 2-D X-ray shadow images taken by progressively rotating the physical GDL specimen by 0.9°. For this study, the imaging process is carried out on an uncompressed GDL sample as manufactured. Nanotomography images are generated using a Skyscan 2011 system, which contains an X-ray source of 25 kV at 200 μA. The shadow images are collected using an X-ray camera which contains a scintillator and a charged couple device (CCD) chip of 1024 $\times$ 1024 pixel resolution with 12-bit depth. The object diameter is approximately 0.7 mm which gives a maximum resolution of 0.68 nm.

The 2-D X-ray shadow images are subsequently compiled using CTAN software to generate a stack of 2-D grayscale images in 256 shades of gray. A previously-reported thresholding process is then applied to the 2-D images in order to define the partition on the grayscale which divides the shades of gray that correspond to void space to those that correspond to solid space.[14,15] The determined threshold is then applied to the entire stack of 2-D images.

The final step is a computational one which translates the stack of threshold 2-D images into a complete 3-D digital model of the GDL structure where each voxel has a resolution of 680 $\times$ 680 $\times$ 680 nm^3 and contains either a 1 to depict solid space, or 0 for void space. This is carried out using the Double Time Cubes/Marching Cubes algorithm.[16]

Table 1. Image Sizes for the Reconstructed and Selected Regions of the Carbon Paper GDL from X-ray and Nanotomography

	Reconstructed Region		Selected Region for LB Modelling	
Image size	Pixels	Length, μm	Pixels	Length, μm
x-direction	920	736	145	98.6
y-direction	900	720	145	98.6
z-direction	325	260	40	27.2
Porosity	0.89		0.76	

Each voxel is used directly as a computational element in the LB model without modification.

Table 1 summarizes the pixel and geometric sizes of the reconstructed 3-D digital model and the region of that which is used for the numerical study. Figure 1a shows the full digital model of the sample acquired while Figure 1b shows the region of interest for the LB model; the region of interest for the LB model is located approximately at the center of Figure 1a. The limitation of the current work is that as the 3-D structural model shown in Figure 1b is preselected with a limited thickness to simulate the initial breakthrough of liquid water, the resulting numerical conclusions will not reflect liquid intrusion characteristics through the full thickness of the GDL structure.

Two-phase lattice boltzmann modeling

While several LB model have been developed to simulate two-phase flow,[17,18] that proposed by Shan and Chen[19] is applied for this work for its wide use in the literature and will be referred to as the S-C model in the following. The original S-C model was based on the single relation-time (SRT) approach.[20] Recent work, however, based on single-phase flow revealed that the SRT LB model cannot correctly represent the location of the fluid-solid interface.[21] As a result, when applied to porous media, the permeability that is calculated based on the simulated velocity field at pore scale is not a constant but can vary unrealistically with fluid viscosity.[21] To overcome this limitation, a multiple relaxation-time (MRT) LB model has been developed by transferring the particle distribution functions in the SRT model into a space of moments.[22] Since each moment represents a physical quantity, the MRT model offers a more convenient way to calculate the collision as it can use different relaxation times to relax different physical quantities, and is therefore more robust. In this article, the MRT approach is applied to the S-C model. In the MRT S-C model, each fluid component is modeled by the following equation[23]

$$f_{i,k}(\boldsymbol{x}+\delta t\xi_i, t+\delta t) = f_{i,k}(\boldsymbol{x},t) + \boldsymbol{M}^{-1}\boldsymbol{S}_k\boldsymbol{M}\left[f_{i,k}^{eq}(\boldsymbol{x},t) - f_{i,k}(\boldsymbol{x},t)\right], \tag{1}$$

where $f_{i,k}(\boldsymbol{x}, t)$ is the particle distribution function for fluid k ($k = 1, 2$) at location $\boldsymbol{x}$ and time t, moving with velocity ξ_i; $f_{i,k}^{eq}(\boldsymbol{x},t)$; is the equilibrium distribution function for fluid k, the value of $f_{i,k}(\boldsymbol{x},t)$ at equilibrium state; $\boldsymbol{M}$ is the transform matrix, which is given in[24]; and $\boldsymbol{S_k}$ is a collision matrix. The identity transforms $\boldsymbol{m}_k = \boldsymbol{M}\boldsymbol{f_k}$ the particle distribution functions $\boldsymbol{f_k} = (f_{0,k}, f_{1,k} \sim f_{18,k})$ into moments; the collision matrix $\boldsymbol{S}_k$ for the fluid k is diagonal and its terms are given by

$$\begin{aligned} &s_{0,k} = 0 \\ &s_{3,k} = s_{5,k} = s_{7,k} = 1, \\ &s_{1,k} = s_{2,k} = s_{9,k-15,k} = 1/\tau_k, \\ &s_{4,k} = s_{6,k} = s_{8,k} = s_{16,k-18,k} = 8(2 - 1/\tau_{,k})/(8 - 1/\tau_{,k}). \end{aligned} \tag{2}$$

This ensures the correct recovery of the location of the fluid-solid boundary, and that the collision is only applied to the moments that are not locally conservative.

The kinematic viscosity of fluid k in the aforementioned MRT model is determined by $\mu_k = \delta x^2(\tau_k - 0.5)/6\delta t$, where δx is the size of the cubic voxel, and δt is a time step during which the particle moves from one voxel into another. The macroscopic density for each fluid and the mixture density of the two fluids are calculated, respectively by

$$\rho_k = \sum_{i=0}^{18} f_{i,k}, \tag{3a}$$

$$\rho = \sum_{k}\sum_{i=0}^{18} f_{i,k}, \tag{3b}$$

Fluid-fluid interactions

In the S-C model, the repellent reaction between the two fluids considers only the nearest-neighbor interactions, in which the interactive force imposed by fluid k' to fluid k is calculated as follows ($k' \neq k$)

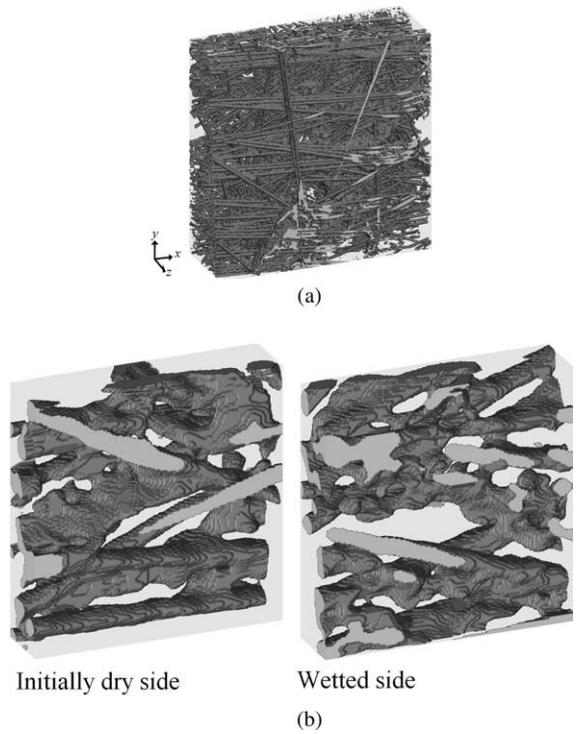

Figure 1. Reconstructed region of carbon paper GDL.

$$\mathbf{F}^k_{f-f}(\mathbf{x}) = -\rho_k(\mathbf{x}) \sum_{k'} G_{\mathbf{kk'}}(\mathbf{x},\mathbf{x}')\rho_{k'}(\mathbf{x}')(\mathbf{x}-\mathbf{x}') \quad (4)$$

where $G(\boldsymbol{x}, \boldsymbol{x}')$ represents the strength of the reaction between the two fluid and is calculated as follows[25]

$$G_{\boldsymbol{kk'}}(\boldsymbol{x},\boldsymbol{x}') = \begin{cases} g_{kk'} & |\boldsymbol{x}-\boldsymbol{x}'| = \sqrt{2}\delta x \\ 2g_{kk'} & |\boldsymbol{x}-\boldsymbol{x}'| = \delta x \\ 0 & \textbf{\textit{otherwise}} \end{cases} \quad (5)$$

where $g_{kk'}$ is a constant $g_{kk'}$. Increasing beyond a critical value could progressively separate the two fluids. The pressure of the mixture of the fluids is given as

$$P(\mathrm{x}) = \frac{\rho_1+\rho_2}{3} + 12 g_{kk'}\rho_1\rho_2 \quad (6)$$

Fluid-solid interactions

The interaction between fluid k in a voxel centered at $\boldsymbol{x}$ with a solid boundary at location $\boldsymbol{x}'$ is modeled by[25]

$$\mathbf{F}_{f-s}(\mathbf{x}) = -\rho_k(\mathbf{x}) \sum_{\mathbf{x}'} G_{ks}(\mathbf{x},\mathbf{x}')(\mathbf{x}-\mathbf{x}') \quad (7)$$

To ensure consistency with the fluid–fluid interaction, the reaction parameter $G_{ks}(\boldsymbol{x},\boldsymbol{x}')$ in Eq. 7 is described by

$$G_{\boldsymbol{ks}}(\boldsymbol{x},\boldsymbol{x}') = \begin{cases} g_{ks} & |\boldsymbol{x}-\boldsymbol{x}'| = \sqrt{2}\delta x \\ 2g_{ks} & |\boldsymbol{x}-\boldsymbol{x}'| = \delta x \\ 0 & \textbf{\textit{otherwise}}. \end{cases} \quad (8)$$

Changing the sign of g_{ks} allows the simulation of hydrophobic and hydrophilic materials. In Eq. 7, $s(x - x')$ is a phase factor in that its value is 1 when the voxel centered at $\boldsymbol{x}'$ is a liquid, and 0 otherwise. If fluid 1 is assumed to be wetting and fluid 2 nonwetting, g_{1s} is positive, and $g_{1s} = -g_{2s}$.

Under the influence of fluid-fluid and fluid-solid interactions, the macroscopic velocity for each fluid is calculated as follows

$$\rho_k \boldsymbol{u_k} = \sum_k \xi_i f_{i,k} + 0.5\left(\boldsymbol{F}^k_{f-f} + \boldsymbol{F}^{\boldsymbol{k}}_{\boldsymbol{f-s}}\right) \quad (9)$$

and the mean velocity of the two fluids as

$$\rho \boldsymbol{u} = \sum_k \rho_k \boldsymbol{u_k} \Big/ \sum_k \rho_k + 0.5 \sum_k \left(\boldsymbol{F}^k_{f-f} + \boldsymbol{F}^k_{f-s}\right) \quad (10)$$

In this article, we used the D3Q19 lattice as described in our previous work[10] which considers 19 fluid velocities at each node in the 3-D lattice; each node represents a center-point of a voxel in the 3-D structural model generated from X-ray tomography. For two-phase flow, the equilibrium distribution functions for fluid k are given by the following in the moment space of $\boldsymbol{m}^{eq}_k = \boldsymbol{M}\boldsymbol{f}^{eq}_k$

$$\begin{aligned}
&m^{eq}_{0,k} = \rho_k, \\
&m^{eq}_{1,k} = -11\rho_k + 19(j^2_{x,k} + j^2_{y,k} + j^2_{z,k}), \\
&m^{eq}_{2,k} = 3\rho_k - 5.5(j^2_{x,k} + j^2_{y,k} + j^2_{z,k}), \\
&m^{eq}_{3,k} = j_{x,k}, m^{eq}_5 = j_{y,k}, m^{eq}_7 = j_{z,k}, \\
&m^{eq}_{4,k} = -2j_{x,k}/3, m^{eq}_6 = -2j_{y,k}/3, m^{eq}_8 = -2j_{z,k}/3, \\
&m^{eq}_{9,k} = (2j^2_{z,k} - j^2_{y,k} - j^2_{z,k})/\rho_0, m^{eq}_{10} = (2j^2_{z,k} - j^2_{y,k} - j^2_{z,k})/, \\
&m^{eq}_{11,k} = (j^2_{y,k} - j^2_{z,k}), m^{eq}_{12} = (j^2_{y,k} - j^2_{z,k}), \\
&m^{eq}_{13,k} = j_{x,k}j_{y,k}, m^{eq}_{13} = j_{x,k}j_{y,k}, , m^{eq}_{15} = j_{x,k}j_{y,k}, /, \\
&m^{eq}_{16,k} = m^{eq}_{17,k} = m^{eq}_{18,k} = 0.
\end{aligned} \quad (11)$$

where j_x,j_y,j_z are the components of the moment $\boldsymbol{j_k} = \rho_k \boldsymbol{u}$.

Simulations and boundary setup

The density and the kinematic viscosity of each of the two fluids are given by Eq. 3a and $\mu_k = \delta x^2(\tau_k - 0.5)/\delta t$, respectively. However, for a water-air system, the density and viscosity ratios of the two fluids are 1:800 and 1:15, respectively, which is beyond the ability of the above LB model because such a high-density ratio makes the model unstable. To determine that water intrusion into the GDLs can be simulated by this model, we calculated the Bond number (ratio of gravitation to interfacial force), capillary number (ratio of viscose force to interfacial force), and Reynolds number (ratio of inertial force to viscose force) of water and air in the GDLs. For an averaged pore diameter of 10 microns in GDLs, the results are given in Table 2, where g is gravitational acceleration, ρ_w and μ_w are the density and viscosity of water, respectively, ρ_a and μ_a are the density and viscosity of air, respectively, σ_{wa} is water-air surface tension, and D is the average pore diameter in the GDL.

The Bond number in Table 2 shows that the impact of gravity is negligible in comparison with capillary; similarly, the capillary number reveals that the viscous force is also negligible in comparison with capillary force; the Reynolds number tells that the inertial force is much smaller than the viscous force and the flow is laminar, indicating that the density difference of the two fluids has little effect on fluids flow. Based on the above analysis, we can conclude that water intrusion into GDLs is predominantly controlled by capillary, and the gravitation and viscosity do not have to be accounted as demonstrated previously by Schaap et al.[27] Following Schaap et al, this work simulates water intrusion into the GDLs by setting the relaxation parameters for both fluids to be $\tau k = 1$; the densities of the two fluids are the same when the capillary pressure is zero.

Apart from fluid viscosity, the aforementioned two-phase LB model also requires the two parameters $g_{kk'}$ and g_{ks} to be predefined, which characterize the surface tension of water and the hydrophobicity of the solid materials, respectively. Since g_{ks} is not practically measurable, in all the simulations, its value is estimated based on the contact angle and the surface tension of the water.

The phase-reaction parameter $g_{kk'}$ controls the surface tension, but there is no theoretical expression for this. For the current work, the surface tension in the lattice domain was calculated indirectly through a bubble test in which the

Table 2. The Dimensionless Bond, and Capillary and Reynolds Numbers

Dimensionless Parameter	Calculation	Values
Bond number	$\frac{g(\rho_w-\rho_a)R^2}{\sigma_{wa}}$	1.6×10^{-4}
Capillary number	$\frac{\mu_w u_w}{\sigma_{wa}}$	2.47×10^{-8} – 1.92×10^{-7}
Reynolds number	$\frac{\rho_w u_w R}{\mu_w}$	2.12×10^{-4} – 1.65×10^{-4}

formations of bubbles of the wetting phase with different diameters were simulated in three dimensions. When a bubble of the wetting phase was assumed to have stabilized, the pressure difference across the interface of the bubble was given by

$$\Delta P = P_n - P_w = 2\gamma/R \tag{12}$$

where P_n is the pressure just outside the bubble, P_w is the pressure just inside the bubble, γ is the surface tension between the two phases, and R is the radius of the bubble. The pressure drop ΔP across the surface of the bubble increases as the radius of the bubble decreases. Simulations were carried out for bubbles with different radii, and the surface tension γ was calculated by linearly fitting the increase in pressure drop ΔP with, giving a surface tension of 0.18 in lattice units.

The contact angle occurs as a combined effect of surface tension and the solid-fluid reaction parameter g_{ks}. Again, there is no theoretical expression for this relationship. The surface tension of water changes with temperature, but in this work it is assumed that water flow occurs under isothermal conditions. Therefore, in the simulations, the surface tension between the two fluids was assumed to be a constant. The formation of a droplet (wetting fluid) on solid plates is then simulated with different values of from which the dependence of the contact angle g_{ks} on can be calculated. As an illustrative example, Figure 2 shows the impact of g_{ks} on the shape of the droplet on a plate. When $g_{ks} = 0$ there is no reaction between solid and fluid and the contact angle is, therefore, 90°; when g_{ks} is negative the plate is hydrophobic and the contact angle is greater than 90°; when g_{ks} is positive, the plate is hydrophilic, and the contact angle is less than 90°. The change of the contact angle with over two values of g_{ks} is shown in Figure 3.

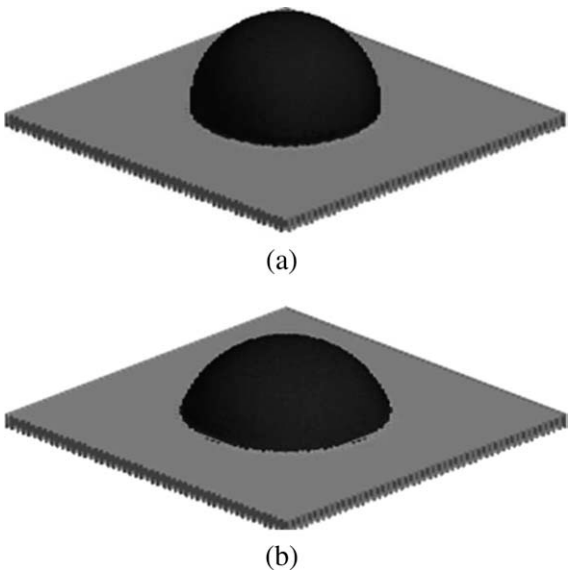

Figure 2. Selected region for two-phase LB simulation.

For the purposes of the current study, the model is designed to simulate water intrusion into a GDL by assuming that capillary action is the dominant mechanism that drives the movement of water. As a result, gravity is neglected and the viscous frictions are assumed to be minor, which permits the freedom to choose relaxation-time parameters that ensure numerical stability. To create suction between the outlet and inlet of the sample, a buffer zone is applied at the top, consisting of 10 layers with the first layer completely filled with air; the buffer zone is hydrophobic. Another buffer consisting of 10 layers is also applied at the bottom with the first layer completely filled with water; the bottom buffer is hydrophilic. Suction is created by differentiating the pressure of air in the top layer and water pressure in the bottom layer, both calculated from Eq. 6. All variables in the LB simulations are in lattice units. The applied suction $P_{c,p}$ in the physical domain is scaled to a suction $P_{c,L}$ in the lattice unit (by suction in) by the following equation

$$P_{c,p} = \frac{P_{c,L}\sigma_P}{\delta x \sigma_L} \tag{13}$$

where σ_P and σ_L are the water surface tension in the physical domain and the lattice unit, respectively.

Results and Discussions

The first test case studied in this work assumes that all surfaces of the solid GDL structure are fully hydrophobic (HB) with a contact angle of 102.5°. The second test case considered a fully hydrophilic (HL) GDL structure with a contact angle of 80°, which corresponds to graphite.[1] Five liquid intrusion pressures were considered for each case; 1 kPa, 3 kPa, 10 kPa, 30 kPa and 100 kPa. Numerical simulations were carried out on a quad-core 2.33 GHz workstation with 3.25 Gbytes of RAM; a single LB simulation at a given liquid intrusion pressure required up to 140 h to reach steady

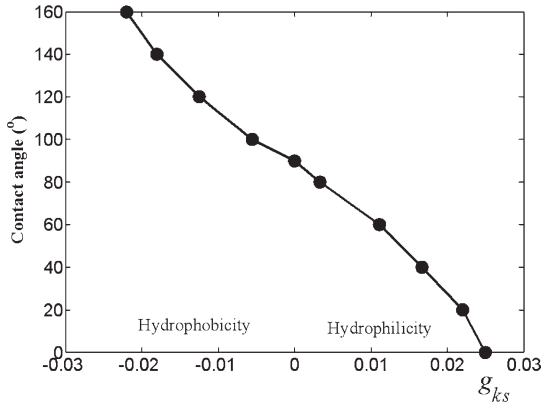

Figure 3. An illustrative example to show the decrease in contact angle with as the value of *g(ks)* increases; (a) = 0.0, contact angle = 90°, and (b) *g(ks)* = 0.01, contact angle = 60°.

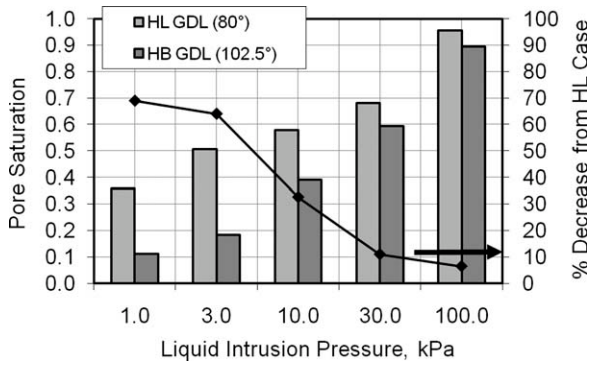

Figure 4. The change of the contact angle with the fluid-solid reaction parameter g_{ks}.

state. The resulting intruded liquid volumes are discussed first, followed by the evolution of liquid breakthrough, and finally the pore-size distribution (PSD).

Volumetric liquid intrusion

Figure 4 shows the relationship between liquid intrusion pressures and pore saturation in the GDL structure at steady-state. The results indicate that as liquid intrusion pressure increases, the change in intruded volume between hydrophobic and hydrophilic porous structure decreases, as indicated by the plotted line. This is as would be expected. The surface energy for a hydrophilic surface is high due to its greater bonding potential, while the opposite is true for a hydrophobic surface. The consequence of this is the expected increase in intruded volume with liquid intrusion pressure for both cases. The greater surface energy in the case of the hydrophilic porous structure enables the corresponding intruded volumes to achieve a higher value than the hydrophilic case because it can;

(a) enter a greater number of interactions with water molecules, which thereby allows more water to adhere to the solid surfaces through the porous structure, and;

(b) simultaneously allows water to infiltrate the porous structure therewith due to the inherent cohesion between water molecules.

As the liquid water proceeds to occupy a greater proportion of the total pore space with increasing intrusion pressure the remaining void space becomes limited, and as such the difference in intruded volumes between the two cases diminishes.

What is most notable is that the molecular interactions between solid and liquid due to adhesion and the cohesion within liquid water plays a large role in determining the water intrusion characteristics at low pressures. At 3 kPa, the pore saturation of the hydrophilic test case is 0.51, but decreases by 64% down to 0.18 for the hydrophobic test case; at 30 kPa, the pore saturation for the hydrophilic test case is 0.68, and decreases by 13% to 0.59 for the hydrophobic case. In effect, therefore, based on average pore saturations of 0.48 and 0.23 in the 1– 10 kPa range for the hydrophilic and hydrophobic cases, respectively, a local porous structure with a contact angle of 80° can on average conduct twice as much liquid water away from a liquid-saturated boundary than one with a contact angle of 102.5°.

Evolution of liquid intrusion

Figures 5–9 show the evolution of liquid saturation for the five liquid intrusion pressures, respectively, for the hydrophobic case (left), and the hydrophilic case (right). The figures visually demonstrate that the liquid front advances deeper into the material for a given intrusion pressure in the hydrophilic case compared to the hydrophobic case for the reasons discussed in the preceding section. The visualization also identifies one dominant pathway in both cases located toward the center of the specimen; Figure 6 shows that the breakthrough of the liquid-water front through this pathway is established with an intrusion pressure of 3kPa in the hydrophilic case. The same phenomenon in the hydrophobic case is not clearly visible until 10kPa. This phenomenon — which occurs as a consequence of the structural features of this region of the GDL — also explains the relatively larger

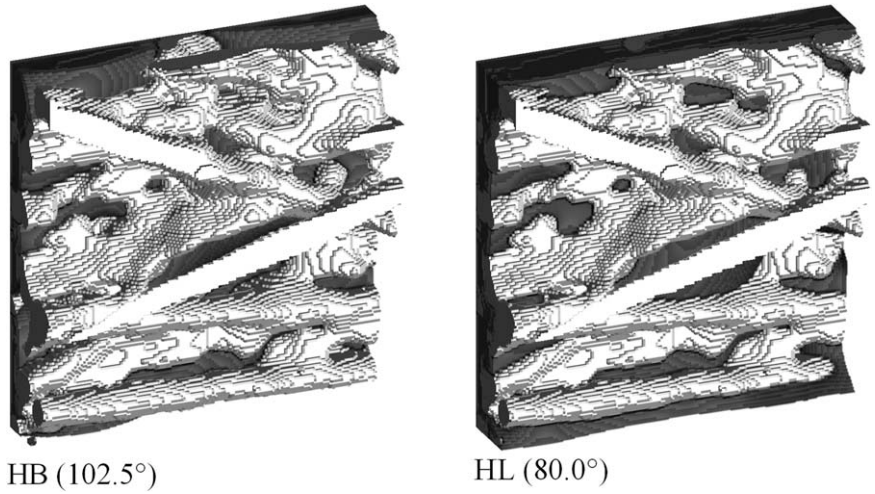

Figure 5. Simulated liquid intrusion volume as a function of liquid intrusion pressure for initial breakthrough in a fully hydrophobic (HB) and hydrophilic (HL) GDL structure (contact angles are shown in brackets).

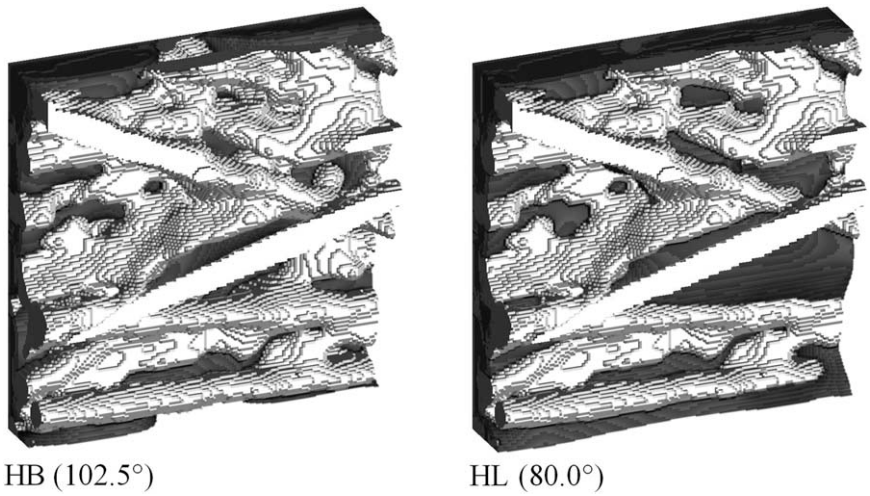

Figure 6. 3-D liquid intrusion at an intrusion pressure of 1kPa.

jump in the intruded volume for the case of the hydrophilic GDL from 1 kPa to 3 kPa, as shown in Figure 4. For the hydrophobic case, however, the breakthrough does not occur and the increase in intruded volume is comparatively lower.

Figures 5–9 also indicate more generally, however, that liquid intrusion does not necessarily proceed through identical pathways in the two cases. Figure 8, for example, demonstrates quite clearly that although the saturation for the hydrophilic case (0.68) is only approximately 15% greater than that for the hydrophobic case (0.59) at 30 kPa, the distributions of liquid water within the structures are notably different; in the hydrophilic case liquid water is vacant in three zones toward the bottom of the structure, yet has proceeded to infiltrate the region to the right of the center, whereas in the hydrophobic case the liquid water is actually occupying the vacant zones, but has not proceeded into the upper-half of the structure in the same manner. Similar characteristics are also evident in Figure 9. Therefore, the results suggest that not only is liquid intrusion a function of the adhesion with the solid surfaces and the cohesion within liquid water, it is also dependant upon the local geometry of the porous network at any given intrusion pressure.

Conclusions

The literature identifies that the lattice Boltzmann numerical model has the potential to reveal the nature of microscopic two-phase flows in fuel-cell materials. This research newly demonstrates the amalgamation of a two-phase 3-D lattice Boltzmann numerical model with a digital microstructural model of an actual carbon paper GDL as manufactured, which is acquired through X-ray nanotomography. The principal conclusions of this work are as follows.

Digital reconstruction of carbon paper GDL via X-ray microtomography

This study applies a previously-developed three-stage imaging technique to reconstruct a 3-D digital model of an uncompressed carbon paper GDL sample. The imaging

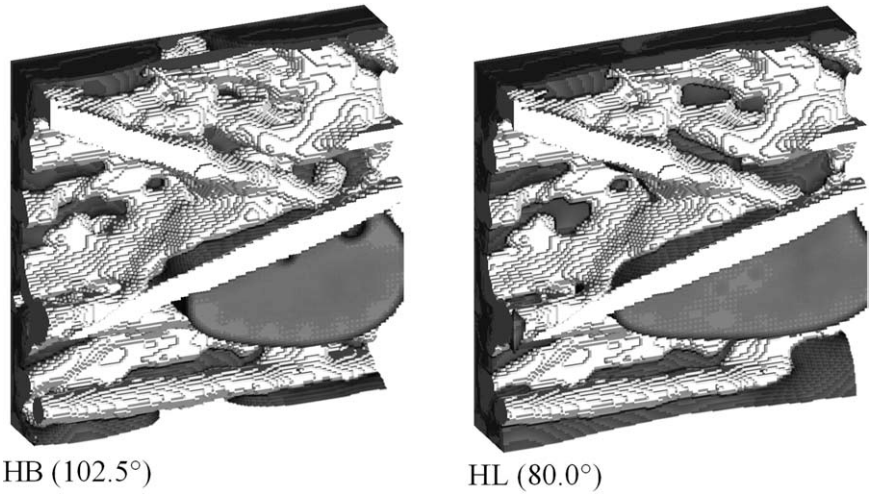

Figure 7. 3-D Liquid intrusion at an intrusion pressure of 3kPa.

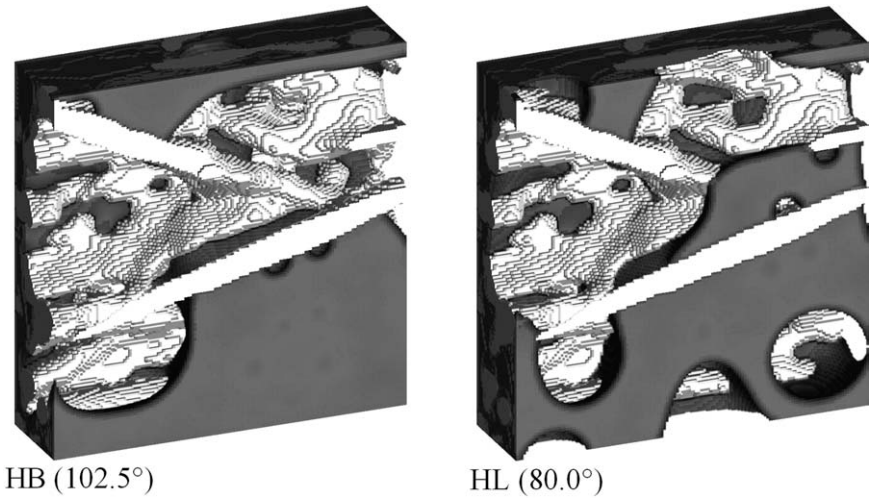

Figure 8. 3-D Liquid intrusion at an intrusion pressure of 10kPa.

process generally involves (a) an initial X-ray imaging step where 2-D shadow images are progressively acquired rotating the sample through 180°, (b) a thresholding step where the 2-D grayscale images are converted into binary images where 1 represents solid space, and 0 represents void space, and (c) a digital reconstruction step which compiles the threshold images into a 3-D digital model of the GDL. A region from the complete digital model is then used for direct numerical modeling.

Two-Phase 3-D lattice Botlzmann numerical modeling

A newly-developed two-phase lattice Botlzmann numerical model has been developed in order to simulate the movement of liquid water through the porous structure of the GDL sample. The model considers 19 velocities for each fluid at each node in the lattice. In applying the model, it is assumed that the surfaces of the GDL structure have a homogeneous and predefined contact angle in order to account for wet proofing properties. In reality, it is likely that any wet proofing agent may infiltrate the GDL structure inhomogeneously rendering the solid surfaces partially hydrophobic and partially hydrophilic. Liquid saturation is simulated for each liquid intrusion pressure and surface contact angle individually. The region of interest supplied from the X-ray imaging process is used directly by the LB model.

The effect of liquid intrusion pressures on intruded volume

This study focuses on three liquid intrusion pressures; 1 kPa, 3 kPa, 10 kPa, 30 kPa and 100 kPa. Simulations are carried out on a single structural model of the GDL assuming that the contact angle of its solid structure is 80° and 102.5°, respectively. The numerical simulations indicate that for any given liquid intrusion pressure, the liquid saturation for the hydrophilic case is greater than that for the hydrophobic case, as expected. In the case of the hydrophobic GDL, the saturation increases from 0.11 – 0.90 over the

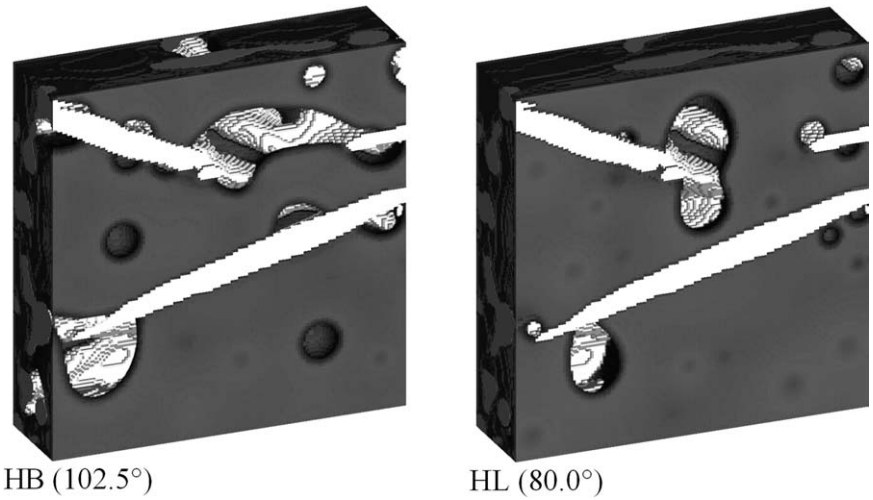

Figure 9. 3-D Liquid intrusion at an intrusion pressure of 30kPa.

given intrusion pressures, whereas for the hydrophilic case the saturation increases from 0.36 – 0.96.

Evolution of pore saturation

The results of the LB numerical modeling are visualized in order to identify the evolution of liquid intrusion. The results indicate that liquid infiltration for the hydrophilic and hydrophobic cases does not strictly proceed along identical pathways for the same intrusion pressures. The visualizations generally reveal a substantial breakthrough at 10 kPa through an identifiable pore, but that much of the subsequent movement of water leaves significantly different water distribution patterns.

It is notable that while some of the fluidic characteristics captured by this work are specific to the structure of the GDL chosen for the current analysis, what is of primary importance is that the work newly demonstrates the ability to recreate and examine the movement of liquid water in directly-acquired GDL structures taken from actual fuel-cell materials, which would otherwise be formidable to capture via *in situ* measurement. The treatment of inhomogeneous hydrophobicity within the GDL could be addressed through elemental mapping. It is, for example, possible to mill a pocket in a GDL sample and polish its walls with a low-current focused ion beam (FIB). Energy-dispersive X-ray spectroscopy (EDS) with scanning electron microscopy (SEM) can then be applied to locate fluorine on the walls, which theoretically can be correlated to a contact angle. While this study elucidates some basic characteristics of liquid infiltration in GDL structures, the feasibility demonstrates that through the current methodology it is now possible to investigate pore-scale liquid flow in actual fuel-cell materials and to a much greater depth than has been permitted in general thus far. It is anticipated that this capability can complement other diagnostics techniques such as neutron imaging in order to holistically understand the mechanisms of two-phase transport in PEFCs.[26]

Acknowledgments

This research was supported by the UK Technology Strategy Board (TSB Project No. TP/6/S/K3032H). We acknowledge industrial partners AVL List GmbH, Intelligent Energy, Ltd., Johnson Matthey Fuel Cells, Ltd., Saati Group, Inc., and Technical Fiber Products, Ltd. for their support of this work.

Notation

D = average pore diameter in GDL
$f_{i,k}$ = particle distribution function for fluid k
$\boldsymbol{F}_{f\text{-}f}$ = fluid–fluid interaction force
$\boldsymbol{F}_{f\text{-}s}$ = fluid-solid interaction force
g = the gravitational acceleration
g_k' = parameter to characterize the surface tension of the fluids
g_{ks} = parameter to characterize the hydrophilicity of fluid k
$\boldsymbol{j}_k$ = macroscopic moment vector of fluid k
$m_{i,k}$ = moment distribution functions for fluid k
$m_{i,k}^{eq}$ = the equilibrium moment distribution function for fluid k
$\boldsymbol{M}$ = the matrix transforms to $f_{i,k}$ to $m_{i,k}$
P = average pressure of the fluid mixture
R = the radius of air bubble
S_k = collision matrix for fluid k
$\boldsymbol{u}_k$ = macroscopic velocity vector of fluid k
$\boldsymbol{x}$ = position coordinate in the LB lattice

Greek letters

δx = side length of the X-ray image voxels
δt = time step
μ_k = kinematic viscosity of fluid k
ξ_i = lattice velocity vector
ρ = density of fluid mixture
ρ_k = density of fluid k
σ_{wa} = surface tension between water and air
σ_L = dimensionless surface tension between water and air
τ_k = parameter characterizes the viscosity of fluid k

Literature Cited

1. Weber AZ. Newman. Modeling transport in polymer-electrolyte fuel cells. *J Chem Rev*. 2004;104(10):4679–4726.
2. Wang CY. Fundamental models for fuel cell engineering. *Chem Rev*. 2004;104(10):4727–4766.
3. Kumbur EC, Sharp KV, Mench MM. Validated Leverett approach for multi-phase transport in polymer electrolyte fuel cell porous media. Part 3: Temperature effect and unified approach. *J. Electrochem. Soc*. 2007;154(12):B1315–B1324.
4. Sinha PK, Mukherjee PP, Wang CY. Impact of GDL structure and wettability on water management in polymer electrolyte fuel cells. *J Mater Chem*. 2007;17:3089–3103.
5. Mukherjee PP, Wang CY. Mesoscopic modelling of two-phase behaviour and flooding phenomenoa in polymer electrolyte fuel cells. *Electrochim. Acta*. 2009;54(27):6861–6875.
6. Niu XD, Munekata T, Hyodo SA, Suga K. An investigation of water-gas transport processes in the gas-diffusion-layer of a PEM fuel cell by a multiphase multiple-relaxation-time lattice Boltzmann model. *J Power Sources*. 2007;172:542–552.
7. Koido T, Furusawa T, Moriyama K. An approach to modelling two-phase transport in the gas diffusion layer of a proton exchange membrane fuel cell. *J Power Sources*. 2008;175:127–136.
8. Park J, Li X. Multi-phase micro-scale flow simulation in the electrodes of a PEM fuel cell by lattice Boltzmann method. *J Power Sources*. 2008;178:248–257.
9. Hao L, Cheng P. Lattice Boltzmann simulation of liquid droplet dynamic behaviour on a hydrophobic surface of a gas flow channel. *J Power Sources*. 2009;190:435–446.
10. Rama P, Liu Y, Chen R, Ostadi H, Jiang K, Zhang X, Fisher R, Jeschke M. An x-ray tomography based lattice boltzmann simulation study on gas diffusion layers of polymer electrolyte fuel cells. *J Fuel Cell Sci Technol*. 2010;7(3):031015–031026.
11. Rama P, Liu Y, Chen R, Ostadi H, Jiang K, Gao Y, Zhang X, Grassini P, Brivio D. Determination of the anisotropic permeability of a carbon cloth gas diffusion layer through X-ray computer microtomography and single-phase lattice Boltzmann simulation. *Int J Numer Meth Fluids*. 2010. DOI:10.1002/fld.2378.
12. Rama P, Liu Y, Chen R, Ostadi H, Jiang K, Gao Y, Zhang X, Brivio D, Grassini P. Determination of the anisotropic permeability of a carbon cloth gas diffusion layer through X-ray computer micro-tomography and single-phase lattice Boltzmann simulation. *Fuel Cells*. 2010. DOI: 10.1002/fuce201000037.
13. Rama P, Liu Y, Chen R, Ostadi H, Jiang K, Gao Y, Zhang X, Fisher R, Jeschke M. Multi-scale modelling of single-phase multi-component transport in the cathode gas diffusion layer of a polymer electrolyte fuel cell. *Energy Fuels*. 2010;24(5):3130–3143.
14. Ostadi H, Rama P, Liu Y, Chen R, Zhang XX, Jiang K. Influence of threshold variation on determining the properties of a polymer electrolyte fuel cell gas diffusion layer in X-ray nano-tomography. *Chem Eng Sci*. 2010;65(6):2213–2217.
15. Ostadi H, Rama P, Liu Y, Chen R, Zhang XX, Jiang K. Threshold fine-tuning and 3D characterisation of porous media using x-ray nanotomography. *Current Nanosci*. 2010;6(2):226–231.
16. Skyscan Microtomography. *CT-Analyser Users Guide, Version 1.6.1*. 2007;19–65.
17. He XY, Chen SY, Zhang RY. A lattice Boltzmann scheme for incompressible multiphase flow and its application in simulation of Rayleigh-Taylor instability. *J Comput Phys*. 1999;152(2):642–663.

18. Swift MR, Orlandini E, Osborn WR, Yeomans JM. Lattice Boltzmann simulations of liquid-gas and binary fluid systems. *Phys Rev E*. 1996;54(5):5041–5052.
19. Shan XW, Chen HD. Lattice Boltzmann model for simulating flows with multiple phases and components. *Phys Rev E*. 1993;47(3): 1815–1819.
20. Qian YH, d'Humieres D, Lallemand P. Lattice BGK models for Navier-Stokes equation. *Europhys Lett*. 1992;17(6):479–484.
21. Pan CX, Luo LS, Miller CT. An evaluation of lattice Boltzmann schemes for porous medium flow simulation. *Comput Fluids*. 2006;35(8–9):898–909.
22. Lallemand P, Luo LS. Theory of the lattice Boltzmann method: Dispersion, dissipation, isotropy, Galilean invariance, and stability. *Phys Rev E*. 2000;61(6):6546–6562.
23. Li HN, Pan CX, Miller CT. Pore-scale investigation of viscous coupling effects for two-phase flow in porous media. *Phys Rev E*. 2005;72(2).
24. d'Humieres D, Ginzburg I, Krafczyk M, Lallemand P, Luo LS. Multiple-relaxation-time lattice Boltzmann models in three dimensions. *Philos Trans R Soc Lond Ser A Math. Phys Eng Sci*. 2002; 360(1792):437–451.
25. Martys NS, Chen HD. Simulation of multicomponent fluids in complex three-dimensional geometries by the lattice Boltzmann method. *Phys Rev E*. 1996;53(1):743–750.
26. Bazylak A. Liquid water visualization in PEM fuel cells: A Review. *Int J Hydrogen Energy*. 2009;34(9):3845–3857.
27. Schaap MG, ML Porter, BSB Christensen, D Wildenschild. Comparison of pressure-saturation characteristics derived from computed tomography and Lattice Boltzmann simulations. *Water Resour Res*. 2007;43:W12S06.

Manuscript received Aug. 31, 2010, and revision received Jan. 18, 2011.